Frequency Adaptive ADRC-based Current Control for Grid-connected Inverters in Weak Grids

Qiangsong Zhao, *Member*, *IEEE*, Yuming Zhang, Yuanqing Xia, *Fellow, IEEE*, Ji-Feng Zhang, *Fellow, IEEE*, Jun Wang, and Xu Fang

***Abstract*—Traditional active disturbance rejection control (T-ADRC) schemes for grid-connected inverters (GCIs) face challenges in reference tracking accuracy and harmonic disturbance rejection under grid frequency fluctuations, due to the limited observer bandwidth and phase lag issues. To solve these problems, this paper proposes a frequency-adaptive ADRC (FA-ADRC) scheme, integrating a frequency-adaptive repetitive controller-based extended state observer (FA-RC-ESO) and a frequency-adaptive quasi-proportional-resonant (FA-QPR) controller. The FA-RC-ESO employs an infinite impulse response (IIR) filter to enhance harmonic disturbance estimation, while the FA-QPR achieves zero-phase shift and unity gain for accurate reference tracking. Additionally, the observer bandwidth is optimized by designing zero-phase low-pass filter in the internal model of repetitive control (RC), and the sensor-induced high-frequency noise is effectively suppressed. Theoretical analysis confirms both stability and frequency adaptability of the proposed FA-ADRC. Experimental tests on a 1.5-kW single-phase GCI demonstrate superior performance: precise reference tracking, improved harmonic suppression, and enhanced frequency adaptive capability.**

***Index Terms*—Grid-connected inverter, active disturbance rejection control, repetitive control, extended state observer, frequency adaptive.**

I. Introduction

With the large-scale integration of distributed power generation systems, modern power grids are increasingly exhibiting weak grid characteristics, including severe voltage distortion [1], uncertain grid impedance [2], and grid frequency fluctuations [3]. The single-phase grid-connected inverter (GCI), serving as a key interface between distributed power generation systems and the grid, is required to inject high-quality current into the grid [4]. According to IEEE Std. 519-2022 [5], the total harmonic distortion (THD) of the injected current must remain below 5% in the medium- and low-voltage distribution systems. However, the distorted grid voltage contains a large number of high-frequency harmonic disturbances. In weak grid conditions, the injected current quality of the GCI is severely degraded by the harmonic disturbance and other non-ideal factors [6]. To address these challenges, various advanced control schemes are proposed for GCIs. Model predictive control (MPC) can handle multivariable constraints and achieve fast dynamic response. However, the grid impedance uncertainty in the weak grid can affect model accuracy, causing steady-state performance deterioration under parameter mismatches and model uncertainties [7]. Repetitive control (RC) and quasi-resonant (QR) control are effective in suppressing periodic harmonic disturbances, yet their performance typically degrades under grid frequency fluctuations. These drawbacks highlight the need for a control schemes with enhanced robustness and strong disturbance rejection capability, particularly in weak-grid conditions.

Among various disturbance rejection control schemes [8]–[11], active disturbance rejection control (ADRC) has been increasingly adopted in the GCI systems due to its strong disturbance rejection capability and model-free characteristics [11]. In [12], a first-order linear ADRC incorporating the Padé approximation is applied to a third-order GCI system to address parameter variations and external disturbances. In [13], a first-order linear ADRC with reference differential feedforward is implemented in the GCI system, reducing the phase lag of the injected current.

However, the traditional ADRC (T-ADRC) schemes has a phase lag at the frequency of the reference tracking current, which inevitably results in an undesirable steady-state error. Moreover, the disturbance estimation accuracy of the ESO is critical to the disturbance rejection performance of ADRC. Due to inherent limitations, the observation bandwidth of traditional ESO is constrained by noise frequencies, leading to degraded estimation performance for high-frequency periodic disturbances. Consequently, the T-ADRC schemes with conventional ESO theoretically suffers from poor harmonic disturbance suppression and periodic reference tracking, due to its fixed-bandwidth observer design.

To ensure high-quality injected current, GCIs need to maintain achieve both high-accuracy reference current tracking and effective harmonic rejection, particularly in weak grid conditions. To improve the control performance of the T-ADRC in handling periodic signals, various enhanced ADRC schemes have been developed from two perspectives: (1) improving the reference tracking accuracy, and (2) enhancing

This work was supported in part by the National Natural Science Foundation of China under Grants 62441315 and 62433020, and in part by the Natural Science Foundation of Henan under Grant 252300421299, and in part by the Key Research and Development Projects in Henan Province under Grant 251111220900, and in part by the 2023 outstanding scientific and technological innovation talent support program of Zhongyuan University of Technology under Grant K2023YXRC03. (Corresponding author: Yuanqing Xia.)

Qiangsong Zhao, Yuming Zhang, Yuanqing Xia, and Ji-Feng Zhang are with the School of Automation and Electrical Engineering, Zhongyuan University of Technology, Zhengzhou 450007, China (e-mail: zhaoqiangsong@zut.edu.cn; zhangyuming@zut.edu.cn; xia_yuanqing@bit.edu.cn; jif@iss.ac.cn).

Jun Wang and Xu Fang are with Henan Xuji Instrument Co., Xuchang, Henan 461143, China (wangjun@xj.cee-group.cn; fangxu@xj.cee-group.cn)

0000–0000/00$00.00 © 2021 IEEE

the disturbance estimation accuracy for harmonic disturbances.

Improved reference tracking accuracy is typically achieved by integrating internal model controllers, such as, resonant controller, iterative learning control (ILC), and repetitive control (RC), into the ADRC control law. In [14]–[17], the quasi-resonant controllers are added into the control law of the ADRC to suppress the periodic disturbance with specific frequencies. In [18], an ADRC scheme combined with ILC is proposed for a piezoelectric actuator to simultaneously mitigate both aperiodic and periodic disturbances, enhancing robustness and tracking performance. In [19], a resonant sliding mode controller is embedded into the control law to attenuate both harmonic and unknown disturbances, thereby improving current tracking accuracy and disturbance rejection capability. However, in the aforementioned ADRC schemes based on modified control laws, reference tracking and harmonic disturbance rejection remain coupled, which imposes a limitation on achievable control performance.

The enhanced disturbance estimation accuracy for periodic disturbances is commonly achieved by improving the ESO structure, such as the higher-order generalised ESO [20], [21] and internal model controller-based ESO [14], [22]–[24]. Although the generalized ESO method enhances disturbance estimation accuracy by increasing the observer order, its observation bandwidth remains limited by noise frequency, and it can only accurately estimate a limited number of low-frequency sinusoidal disturbances. In internal model controller-based ESOs, periodic disturbance estimation accuracy is improved by incorporating internal model controllers. Nevertheless, it leads to increased structural complexity and challenging parameter tuning.

To further enhance the estimation accuracy of periodic disturbance, an RC-based ESO (RC-ESO) has been introduced in [24] for permanent magnet synchronous motors, effectively reducing current harmonics in RC-ESO-based ADRC (RC-ESO-ADRC) systems. However, the RC-ESO suffers from a slow convergence rate due to the poles distribution of the RC lying on the boundary of the unit circle in the z-plane. To solve this problem, in [6], a novel RC-ESO (NRC-ESO) based on an ideal compensator is proposed, where the RC poles are distributed at the center of the unit circle, improving the convergence rate of harmonic disturbance estimation. Nevertheless, a critical limitation remains grid frequency fluctuations commonly occurring in weak grids. The above-mentioned RC-ESO schemes are highly sensitive to such frequency fluctuations, leading to a significant deterioration in the estimation accuracy of the harmonic disturbances.

In practice applications, an effective current control scheme should simultaneously accomplish reference tracking and address disturbance rejection to ensure both accuracy and robustness. Although the resonant controllers are embedded into the control law in [15] to enhance current tracking performance, the degradation of tracking accuracy under the grid frequency fluctuations has not been thoroughly addressed. Furthermore, the control schemes based on RC-ESO-ADRC [23]–[27] can improve the disturbance estimation accuracy. However, the estimation accuracy of the RC-ESO for harmonic disturbances is significantly affected by grid frequency fluctuations, thereby compromising harmonic disturbance rejection performance.

In the fixed sampling frequency conditions, fractional-order RC employs finite impulse response (FIR) or infinite impulse response (IIR) filter-based fractional delay filters to dynamically align the controller's resonant frequencies with dominant harmonic components. Unlike FIR filters, well-designed IIR filters can maintain near-unity gain in the pass-band, allowing designers to focus primarily on phase response optimization. Moreover, IIR filters can achieve comparable bandwidth performance with significantly lower filter orders [28]. However, existing literature lacks RC-ESOs have not yet adopted IIR-based fractional-order filtering techniques for frequency-adaptive disturbance estimation.

To address the limitations of conventional RC-ESO-ADRC in handling grid-frequency variations, this paper proposes a frequency adaptive ADRC (FA-ADRC) for single-phase GCIs, combining a Frequency-Adaptive RC-ESO (FA-RC-ESO) and a Frequency-Adaptive Quasi-PR (FA-QPR) controller. The main contributions of this paper are summarized as follows:

1) A novel FA-ADRC scheme is proposed for single-phase GCIs to enhance the reference tracking accuracy and improve the harmonics disturbance rejection performance under grid frequency fluctuations.
2) A new FA-RC-ESO based on an IIR filter is developed to improve the estimation accuracy of RC-ESO for harmonic disturbances. Furthermore, a novel control law FA-QPR is investigated to reduce the phase lag of the injected current, achieving zero steady state error in reference tracking even with the grid frequency fluctuations.
3) A comprehensive stability analysis and detailed parameter design guidelines of the proposed FA-ADRC system are conducted, and the steady-state performance, harmonic suppression capability, and frequency robustness under weak grid conditions are systematically analyzed and verified.

II. Modeling of Single-phase GCI and Problem Formulation

A. Modeling of the Plant

The topology diagram of the single-phase GCI is shown in Fig. 1, where E_d and u_i are the DC bus voltage and inverter output voltage, respectively; L_1 and L_2 are the inverter-side and grid-side inductances, respectively; C is the filtering capacitance; R is the damping resistance; L_g is the grid impedance; u_g, i_g, and i_{ref} are the grid voltage, injected current, and reference current signals, respectively; u_{PCC} is the voltage at the point of common coupling. The phase-locked loop (PLL) is employed to extract the frequency information of the grid voltage. This information is then combined with the amplitude of the reference current I_{ref} to generate the reference current signal i_{ref}.

In this paper, a passive damping scheme is adopted to guarantee the stability of LCL-filter-based GCI, where a damping resistor R is connected in series with a capacitor. The

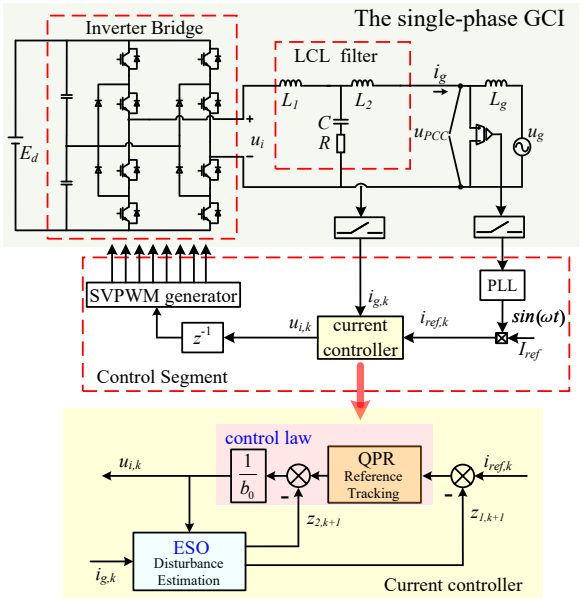

Fig. 1. The topology diagram of the LCL type single-phase GCI

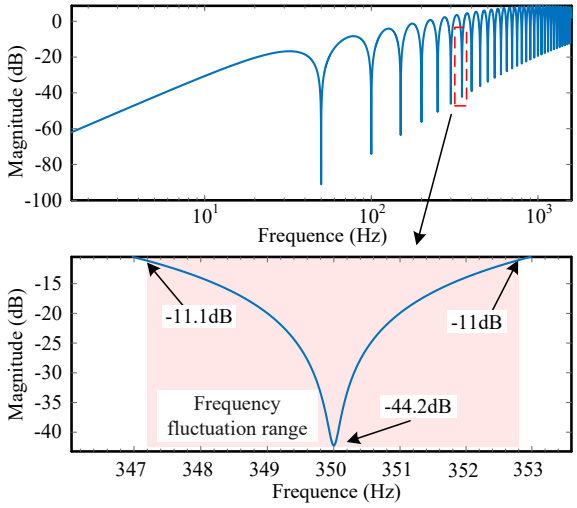

Fig. 2. Amplitude-frequency response of (5).

time-domain expression of the first derivatives of the injected current $i_g(t)$ is $i_g{}'(t)$.

$$\begin{aligned} i_g{}'(t) = &-\frac{L_1L_2C}{(L_1+L_2)}i_g{}'''(t) - RCi_g{}''(t) \\ &+ \frac{CL_1}{(L_1+L_2)}u_g{}''(t) + \frac{RC}{(L_1+L_2)}u_g{}'(t) \\ &+ \frac{1}{(L_1+L_2)}u_g(t) + \frac{RC}{(L_1+L_2)}u_i{}'(t) + bu_i(t) \end{aligned} \tag{1}$$

where $i_g{}''(t)$ and $i_g{}'''(t)$ are the second and third derivatives of the injected current $i_g(t)$, respectively; $u_g{}'(t)$ and $u_g{}''(t)$ are the second and third derivatives of the grid voltage $u_g(t)$, respectively; $u_i{}'(t)$ is the first derivative of the inverter-side voltage $u_i(t)$. The input gain of the system is $b = 1/(L_1+L_2)$. However, since the values of L_1 and L_2 cannot be accurately identified, b is replaced by a nominal value b_0, and the deviation $b-b_0$ is treated as part of the generalized disturbance.

To facilitate analysis, the third-order model of an LCL-type GCI can be approximated by a first-order equivalent system [11]. The modeling uncertainties can be regarded as internal disturbance, which are estimated in real-time by the ESO and compensated by the ADRC control law. The reduced model can be expressed as follows

$$i_g{}'(t) = f(t) + b_0u_i(t) \tag{2}$$

where

$$\begin{aligned} f(t) = &-\frac{L_1L_2C}{L_1+L_2}i_g{}'''(t) - RCi_g{}''(t) \\ &+ \frac{CL_1}{L_1+L_2}u_g{}''(t) + \frac{CR}{L_1+L_2}u_g{}'(t) + \frac{1}{L_1+L_2}u_g(t) \\ &+ \frac{RC}{L_1+L_2}u_i{}'(t) + (b-b_0)u_i(t). \end{aligned} \tag{3}$$

According to (3), the generalized disturbance $f(t)$ contains multiple periodic components, such as the fundamental signal and harmonic disturbance signals. It is worth highlighting that the control performance of ADRC is determined by the observation accuracy of ESO for these periodic signals.

B. Frequency Robustness Analysis of Conventional RC-ESO

To evaluate the frequency robustness of the conventional RC-ESO, this paper employs a frequency-domain analysis approach. Its mathematical representation is as follows

$$\begin{cases} e_{1,k+1}(z) = i_{g,k}(z) - z_{1,k}(z) \\ z_{1,k+1}(z) = z_{1,k}(z) + T_s[z_{2,k}(z) + b_0u_k(z) + \beta_1e_{1,k}(z)] \\ z_{2,k+1}(z) = e_{1,k}(z)G_{rc}(z) + e_{1,k}(z)\Delta G(z) \end{cases} \tag{4}$$

where $i_{g,k}(z)$ is the actual injected current; $z_{1,k}(z)$ is the estimated injected current; $e_{1,k}(z)$ is the estimation error; $z_{2,k}(z)$ is the estimated disturbance; T_s is the sampling time; β_1 is the observer gain; $G_{rc}(z)$ is the RC component. Depending on the type of RC-ESO, $\Delta G(z)$ is usually selected as a proportional gain, an integrator, or a low-pass filter [6], [23], [24].

From (4), the disturbance estimation accuracy of the RC-ESO depends on both $G_{rc}(z)$ and $\Delta G(z)$. When the grid frequency fluctuates, the resonant frequencies of the repetitive controller deviate from the actual harmonic frequencies [29], degrading the harmonic estimation accuracy.

According to [6], the transfer function of the disturbance estimation error in the RC-ESO is expressed as follows

$$\frac{e_{2,k}(z)}{f_k(z)} = \frac{z-1}{z^2 - z + T_sG_{rc}(z)} \tag{5}$$

where $e_{2,k}(z)$ is the disturbance estimation error and $f_k(z)$ is the generalized disturbance.

The amplitude-frequency response of (5) is shown in Fig. 2. When the grid frequency fluctuates within ±0.4 Hz around 50 Hz, the frequency deviation of the D-th order harmonic component will be approximately ±(0.4 × D) Hz. Specifically, for the 7th harmonic, this corresponds to a frequency shift of ±2.8 Hz around 350 Hz, resulting in a fluctuation range from 347.2 Hz to 352.8 Hz as indicated by the shaded region

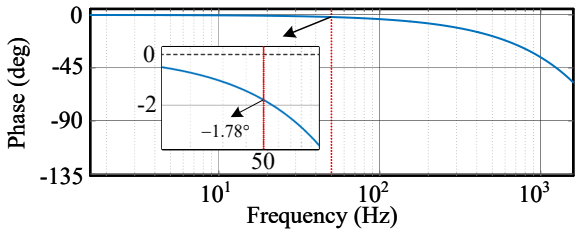

Fig. 3. The phase-frequency response of (6).

in Fig. 2. A lower amplitude-frequency gain indicates to a stronger disturbance estimation capability. As shown in Fig. 2, the gain of the RC-ESO for the 7th harmonic estimation error decreases from -44.2 dB at the nominal 350 Hz to -11.1 dB at 347.2 Hz and -11.0 dB at 352.8 Hz, corresponding to a reduction exceeding 30 dB. These results demonstrate that the disturbance estimation capability of the RC-ESO is significantly compromised during grid frequency fluctuations.

Remark 1: The disturbance estimation accuracy of the RC-ESO is significantly degraded under grid frequency fluctuations, which deteriorates the overall control performance of the ADRC.

C. Reference Tracking Analysis

The proportional control law is widely used in most existing RC-ESO based ADRC schemes. However, this approach cannot achieve zero steady-state error in tracking periodic reference signals. According to [24], the closed-loop transfer function from reference input to system output is given as follows

$$G_{i_{ref,k}}^{i_{g,k+1}}(z) = \frac{k_c T_s}{k_c T_s + z - 1}. \tag{6}$$

The phase-frequency response of (6) is shown in Fig. 3. Note that a small phase lag of the injected current leads to significant steady-state errors. As shown in Fig. 3, when using proportional control law, there is a 1.78° phase lag between reference and injected current. This inherent phase lag fundamentally prevents zero-error tracking of periodic signals in the RC-ESO-ADRC system. To maintain high tracking accuracy dring grid frequency fluctuations, the control law should incorporate the mathematical model of the reference signal and possess frequency-adaptive capability.

Remark 2: The RC-ESO-ADRC scheme exhibits an inherent phase lag when tracking periodic reference signals, such as 50±0.5 Hz sinusoidal waveforms, which fundamentally prevents zero-error tracking.

III. FA-ADRC DESIGN AND ANALYSIS

The analysis in Section II identifies two fundamental limitations in current RC-ESO-ADRC schemes: (a) The disturbance rejection performance is significantly degraded when grid frequency fluctuates; (b) when using proportional control law, the RC-ESO-ADRC scheme exhibits inherent phase lag.

To address the aforementioned issues, a novel FA-ADRC scheme is proposed, whose controller structure is shown in Fig. 4. The FA-ADRC consists of two parts: (1) the FA-RC-ESO to enhance disturbance suppression under grid frequency fluctuations, and (2) the FA-QPR to improve the reference signal tracking accuracy.

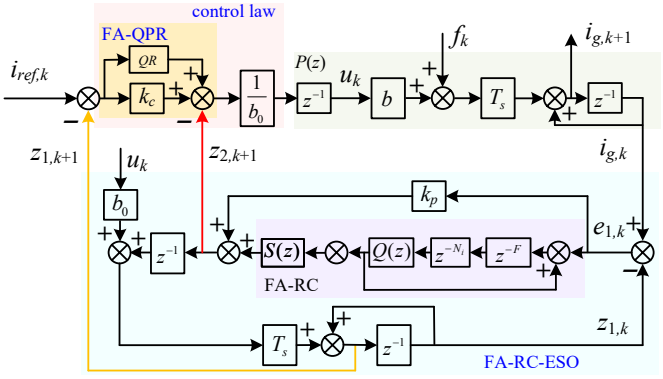

Fig. 4. The discrete diagram of the proposed FA-ADRC scheme.

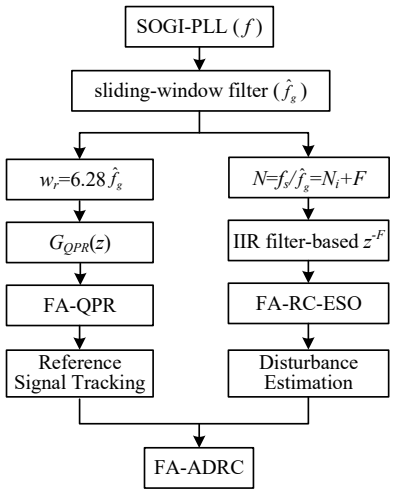

Fig. 5. The frequency adaptation mechanism of the FA-ADRC.

The frequency adaptation mechanism of the FA-ADRC is implemented as shown in Fig. 5. Firstly, the FA-ADRC scheme extracts the initial grid frequency f using a second-order generalized integrator-based phase-locked loop (SOGI-PLL), and then enhances its accuracy through a sliding-window filter to obtain a smoothed and more precise frequency $\hat{f}_g$. $\hat{f}_g$ is used to tune the resonant frequency of the QPR, thereby improving the tracking accuracy for periodic reference signals. Moreover, $\hat{f}_g$ is utilized to calculate the non-integer delay order F, which is approximated by an IIR filter to enhance the disturbance estimation capability of the ESO under grid frequency fluctuations.

A. Design of the FA-RC-ESO

The FA-RC-ESO incorporates an IIR filter based on the Thiran approximation to implement a fractional delay (FD) filter. As shown in Fig. 4, its discrete-time model is expressed

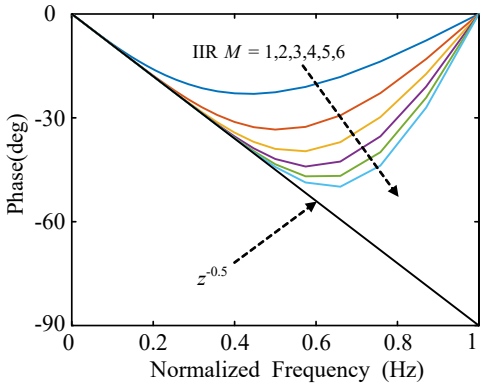

Fig. 6. The phase-frequency responses of the IIR filter.

as

$$\begin{cases} z_{1,k+1}(z) = z_{1,k}(z) + T_s[b_0 u_k(z) + z_{2,k}(z)] \\ z_{2,k+1}(z) = G_1(z)[i_{g,k}(z) - z_{1,k}(z)] \\ G_1(z) = k_p + \dfrac{Q(z)S(z)z^{-N_i}z^{-F}}{1 - Q(z)z^{-N_i}z^{-F}} \end{cases} \tag{7}$$

where $Q(z)$ is a zero-phase low-pass filter, $S(z)$ is the repetitive control compensator, z^{-N_i} is the integer delay component, z^{-F} is the fractional delay component, and k_p is the proportional gain.

1) Design of IIR filter:

When the grid frequency $f_g = 50$ Hz and the sampling frequency $f_s = 10$ kHz, the RC order $N = f_s/f_g$ is an integer. When the grid frequency fluctuates, N may be an non-integer, and can be decomposed into $N = N_i + F$, where N_i is the integer part of the RC order and F is the noninteger part. To approximate the noninteger delay z^{-F}, an IIR filter is utilized. The transfer function $H(z)$ of the IIR filter is expressed as

$$\begin{aligned} z^{-F} &\approx H(z) \\ &= \frac{a_n + a_{n-1}z^{-1} + \ldots + a_1 z^{-(M-1)} + z^{-M}}{1 + a_1 z^{-1} + \ldots + a_{n-1}z^{-(M-1)} + a_n z^{-M}} \end{aligned} \tag{8}$$

where a_n is the coefficient of the all-pass IIR filter used for FD approximation. a_n can be written as

$$a_n = (-1)^n \binom{M}{n} \prod_{m=0}^{M} \frac{F - M + m}{F - M + n + m} \tag{9}$$

where $n = 0, 1, 2, \ldots, M$, and M is the order of the filter. $\binom{M}{n} = \frac{M!}{n!(M-n)!}$ is a binomial coefficient, $F = M + d$, d is the fractional delay parameter. When $-0.5 \le d \le 0.5$, the range of F is optimal [30]. In addition, the stability of the IIR filter needs to be considered. The IIR filter is stable only for $F > M - 1$ [29]. When F is within the optimal range, $F > M - 1$ always holds, and thus the IIR filter remains stable.

Using a fractional delay of $d = 0.5$ as an example, Fig. 8 shows the phase response of IIR filters approximating $z^{-0.5}$ for filter orders $M = 1$ to 6. As shown in Fig. 8, higher-order IIR filters provide a more accurate approximation of the desired fractional delay, while increasing computational complexity. Since injected current harmonics are predominantly confined to the 0-2 kHz band (covering 95% THD), the IIR filter design requires precise magnitude/phase approximation solely within this spectral region Specifically, in Fig. 8, this corresponds to a normalized frequency range of up to 0.4 relative to the sampling frequency. Therefore, considering computational complexity, approximation accuracy, and harmonic suppression range, this paper chooses a third-order IIR filter to approximate the fractional delay. For the given parameters $N = 198.4$ and $M = 3$, the constraint $-0.5 \le d \le 0.5$ is satisfied by setting $N_i = 195$, yielding $d = 0.4$ and $F = 3.4$.

2) Design of the compensator $S(z)$:

As defined by the perfect tracking controller [31], the ideal RC system plant requires zero-phase shift and unity gain across all frequencies. The compensator $S(z)$ is therefore designed to bridge the gap between the actual GCI dynamics and this ideal plant. As shown in Fig. 4, the plant $P_0(z)$ of the RC system can be derived as [32]

$$P_0(z) = \frac{T_s}{z^2 - z + k_p T_s}. \tag{10}$$

Thus, $S(z)$ can be written as

$$S(z) = {P_0}^{-1}(z) = f_s z^2 - f_s z + k_p. \tag{11}$$

where $f_s = 1/T_s$.

Remark 3: As the compensator $S(z)$ is embedded within the ESO framework, its dynamics are inherently unaffected by the inverter's parameter variations.

3) Design of $Q(z)$:

The internal model filter $Q(z)$ is typically implemented as either a low-pass filter or a constant value less than 1. When $Q(z)$ is a constant less than 1, the system stability is enhanced, but a steady-state error is introduced. When $Q(z)$ is implemented as a low-pass filter, it improves the stability of the FA-RC-ESO while reducing disturbance estimation errors. Additionally, it attenuates the RC gain at high frequencies, which limits the observer bandwidth and mitigates the impact of high-frequency noise on the observer.

The discrete transfer function of the zero-phase low-pass filter $Q(z)$ is as follows

$$\begin{aligned} Q(z) &= \sum_{i=0}^{k} \alpha_i z^i + \sum_{i=1}^{k} \alpha_i z^{-i} \\ &\alpha_0 + 2\sum_{i=1}^{k} \alpha_i = 1, \alpha_i > 0 \end{aligned} \tag{12}$$

where k is the order of the zero-phase low-pass filter; α_0 and α_i are the filter coefficients.

Since the grid current harmonics are predominantly concentrated below 2 kHz, a zero-phase low-pass filter should accurately track disturbances up to the 40th harmonic order (2 kHz at 50 Hz fundamental frequency). Considering that higher-order zero-phase low-pass filters lead to increased computational complexity, a first-order filter is selected in this paper. Fig. 7 shows the Bode diagram of $Q(z)$ when $k = 1$ and α_0 takes different values. As shown in Fig. 7, when α_0 is 0.4, 0.6, and 0.8, the corresponding cutoff frequencies are approximately 1640 Hz, 2060 Hz, and 3260 Hz, respectively. As α_0 increases, the cutoff frequency of $Q(z)$ increases significantly, which improves the observer capability to track

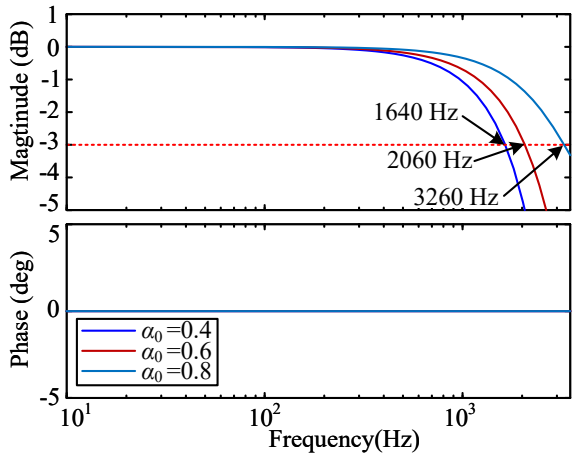

Fig. 7. The Bode diagram of $Q(z)$ for various values of α_0.

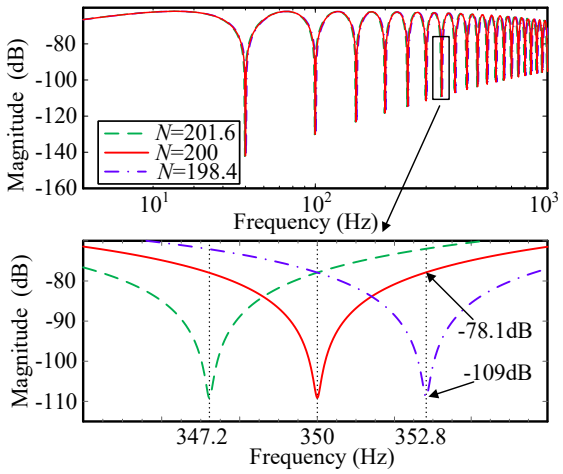

Fig. 8. The amplitude–frequency responses from disturbance to injected current of the FA-ADRC and RC-ESO-ADRC.

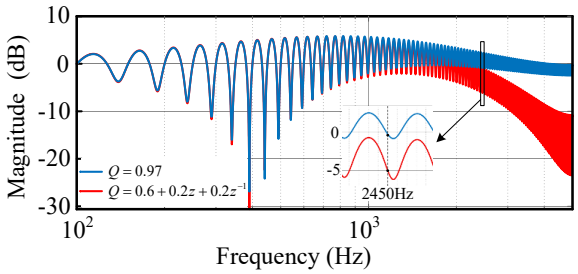

Fig. 9. The amplitude-frequency responses of (13).

low- and mid-frequency disturbances. However, an excessively large α_0 will significantly widen the observer bandwidth, thereby reducing its ability to suppress high-frequency noise. Therefore, the optimal value $\alpha_0 = 0.6$ is selected based on comprehensive performance evaluation in this paper.

B. The Frequency Robustness Analysis

The amplitude-frequency responses of the FA-ADRC and RC-ESO-ADRC system from disturbance to injected current are shown in Fig. 8. In Fig. 8, the solid line represents the amplitude-frequency response when the fundamental frequency is 50 Hz. While the two dashed lines correspond to the amplitude-frequency responses when the fundamental frequency fluctuates to 50±0.4 Hz.

Taking the 7th harmonic as an example, when the grid frequency fluctuates, the disturbance-to-output gain of the system without frequency adaptive mechanism increases from -109 dB to -78.1 dB at 358.2 Hz, resulting in a degradation of approximately 30 dB in disturbance rejection capability. In contrast, the FA-ADRC system maintains a disturbance-to-output gain of -109 dB at 358.2 Hz, demonstrating superior robustness to frequency fluctuations and excellent disturbance rejection performance.

C. The Noise Suppression Analysis

According to [6], the transfer function from measurement noise to the observed current is as follows

$$G_{n_k}^{z_2,k+1}(z) = \frac{T_s G_1(z) z}{z^2 - z + T_s G_1(z)}. \tag{13}$$

For the cases where $Q(z)$ is constant and where a zero-phase low-pass filter is applied, the amplitude-frequency response corresponding to (13) is illustrated in Fig. 9. As shown in Fig. 9, both schemes exhibit similar characteristics in the low-frequency range. However, significant differences emerge at high frequencies. When $Q(z)$ is constant, the observer maintains a high gain at high frequencies, which results in poor attenuation of high-frequency noise. In contrast, when $Q(z)$ is the zero-phase-shift low-pass filter, the observer gain exhibits substantial attenuation at high frequencies. This characteristic effectively suppresses high-frequency noise, thus preventing contamination of the observed current. The zoomed-in view around 2450 Hz further reveals that the zero-phase low-pass filter achieves a lower gain than the constant $Q(z)$ scheme, confirming its superior capability in suppressing high-frequency noise.

D. Design of Control Law Based on FA-QPR

The proportional control law features a simple structure and fast dynamic response, but inherently fails to eliminate steady-state errors when tracking periodic signals. In contrast, the quasi-proportional-resonant (QPR) controller enables accurate tracking of sinusoidal signals within its resonant frequency band. However, due to the fixed resonant frequency of the QPR, any fluctuation in the grid frequency leads to a mismatch between the resonant frequency and the actual signal frequency, resulting in a degraded tracking accuracy. To address this limitation, this paper proposes a frequency-adaptive QPR (FA-QPR), where the resonant frequency dynamically adapts to the grid frequency, ensuring precise tracking of periodic reference signals. The discrete transfer function of the FA-QPR is expressed as follows

$$\begin{aligned} &G_{QPR}(z) \\ &= k_c + \frac{2T_s k_r w_c z^2 - 2T_s k_r w_c z}{z^2 + ({T_s}^2 {w_r}^2 + 2w_c T_s - 2)z - 2T_s w_c + 1} \end{aligned} \tag{14}$$

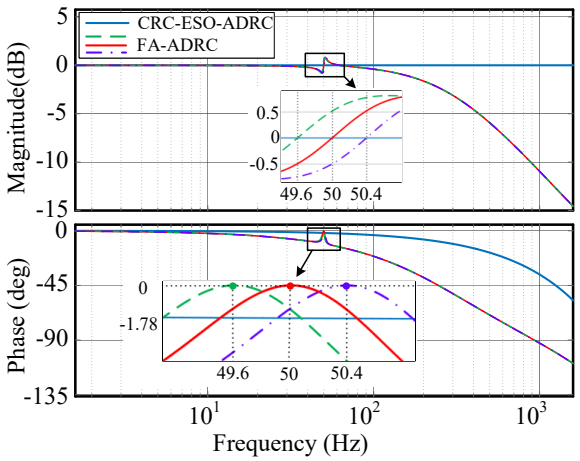

Fig. 10. The Bode diagrams of the RC-ESO-ADRC and FA-ADRC systems under grid frequency fluctuations.

where, w_r is the resonant angular frequency, w_c is the resonant bandwidth of the FA-QPR, k_r is to its resonant gain, and k_c is the proportional gain. Specifically, w_c serves to provide sufficient bandwidth centered on the resonant frequency, k_c ensures the dynamic performance of the system, and k_r is designed to eliminate steady-state error and enhance steady-state performance. Since the FA-QPR can adjust its resonant frequency in real time, the resonant bandwidth w_c does not need to be designed excessively wide. While it only needs to fall within a certain acceptable range. In this paper, the resonant bandwidth is set to $w_c = 3.14$ rad/s. The selection of k_c and k_r will be analyzed and discussed in detail in the parameter design section.

E. Reference Tracking Performance Analysis

When the grid frequency fluctuates, the Bode diagrams of RC-ESO-ADRC and FA-ADRC systems are shown in Fig. 10. As shown in Fig. 10, RC-ESO-ADRC exhibits an inherent phase lag, which impedes zero-error tracking of the reference signal. When the control law adopts a QPR structure, the inherent system delay can be eliminated at its resonant frequency. However, when the grid frequency fluctuates, the resonant frequency of the QPR deviates from the grid frequency, which degrades the tracking performance of the QPR-based system. In contrast, the proposed FA-QPR incorporates frequency adaptation and can track the grid frequency in real time, thereby effectively compensating for phase shifts induced by grid frequency fluctuations. This capability enhances tracking accuracy for periodic reference signals and eliminates steady-state error.

IV. Performance Analysis and Parameter Design of FA-ADRC

A. Stability Analysis of FA-ADRC

As described in [6], the equivalent unit feedback system of the FA-ADRC is shown in Fig. 11.

$$G_c(z) = \frac{G_1(z)}{b_0} \tag{15}$$

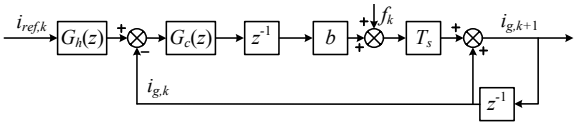

Fig. 11. The equivalent unit feedback diagram of FA-ADRC

$$G_h(z) = G_{QPR}(z)\frac{z^2 - z + T_s G_1(z)}{G_1(z)[G_{QPR}(z)T_s z + z^2 - z]}. \tag{16}$$

When $b_0 = b$, the transfer functions from the reference to the injected current and from the generalized disturbance to the injected current are denoted as $G_{i_{ref,k}}^{i_{g,k+1}}(z)$ and $G_{f_k}^{i_{g,k+1}}(z)$, respectively.

$$G_{i_{ref,k}}^{i_{g,k+1}}(z) = \frac{G_{QPR}(z)T_s}{G_{QPR}(z)T_s + z - 1} \tag{17}$$

$$G_{f_k}^{i_{g,k+1}}(z) = \frac{T_s z^2}{z^2 - z + T_s G_1(z)} \tag{18}$$

According to (17) and (18), $G_{i_{ref,k}}^{i_{g,k+1}}(z)$ only contains the control law parameters, and $G_{f_k}^{i_{g,k+1}}(z)$ only contains the ESO parameters. This shows that the reference tracking performance depends solely on the control law parameters, while the disturbance suppression performance is determined exclusively by the FA-RC-ESO parameters.

Remark 4: The proposed FA-ADRC is a two-degree-of-freedom controller that effectively decouples the reference tracking performance and disturbance suppression performance, thereby simplifying parameter design.

According to the design procedure of the FA-RC-ESO in Section III, by substituting (7), (8), and (11) into (17), the following expression can be derived:

$$G_{f_k}^{i_{g,k+1}}(z) = \frac{T_s z^2[1 - Q(z)z^{-N_i}H(z)]}{z^2 - z + k_p T_s} \tag{19}$$

From (17) and (19), the closed-loop characteristic equation of the system can be expressed as

$$G(z) = [G_{QPR}(z)T_s + z - 1](z^2 - z + k_p T_s) = 0 \tag{20}$$

For discrete-time systems, the system is considered asymptotically stable if all the roots of the closed-loop characteristic equation lie strictly inside the unit circle in the complex plane. According to (14) and (20), the stability of the FA-ADRC is solely determined by the three parameters k_p, k_r, and k_c.

Remark 5: The stability of the FA-ADRC system is independent of the IIR filter and the RC.

B. Parameter Design of FA-ADRC

To facilitate the parameter design, the parameters are set as $k_c = k_{c1} \times b_0$, $k_r = k_{r1} \times b_0$. The pole diagrams corresponding to variations in the control parameters k_{c1}, k_p, and k_{r1} are presented in Fig. 12.

The pole diagram with k_{c1} varying independently as shown in Fig. 12(a). A properly tuned proportional gain k_{c1} can reduce the settling time for the reference signal. However, an excessively large k_{c1} may compromise system instability. As shown in Fig. 12(a), the stable operating range for k_{c1}

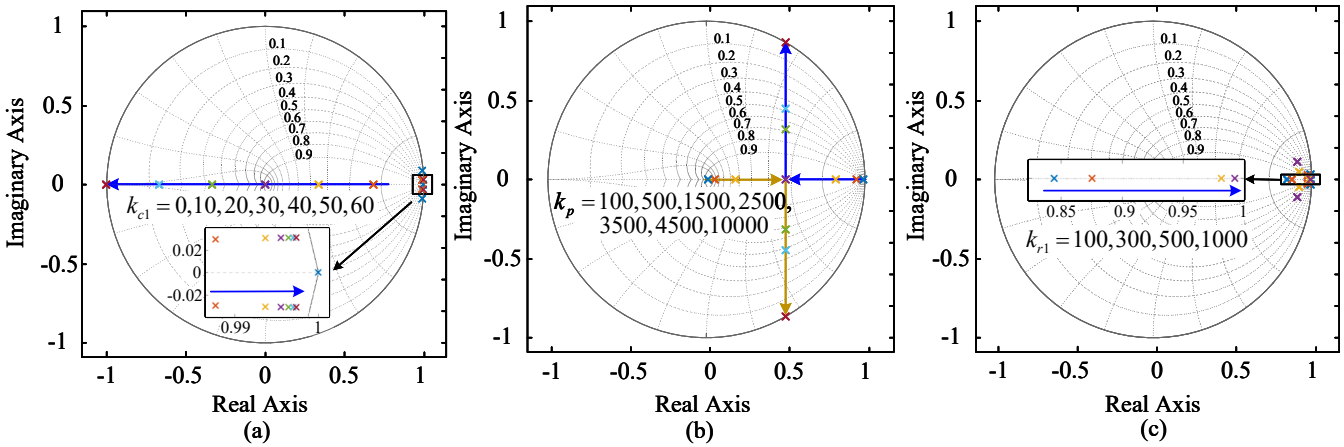

Fig. 12. The closed-loop poles diagrams of FA-ADRC during k_{c1} (a), k_p (b), and k_{r1} (c) change.

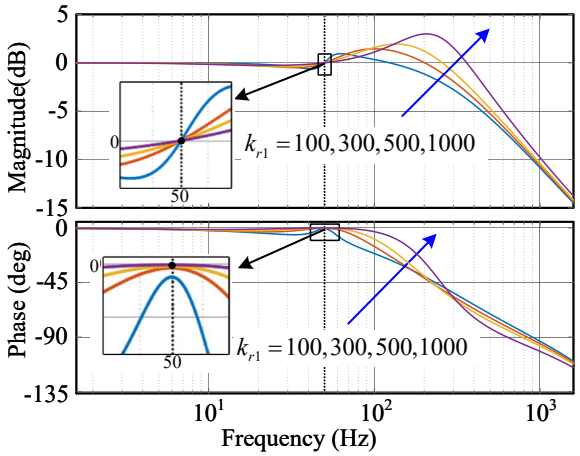

Fig. 13. The bode diagram of FA-ADRC system when k_{r1} changes.

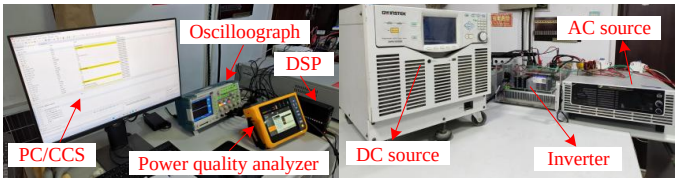

Fig. 14. The single-phase LCL type GCI experimental platform.

TABLE I
PARAMETERS OF SINGLE-PHASE LCL TYPE GCI EXPERIMENTAL PLATFORM

Parameters	Value
Grid voltage u_g	220 V
DC bus voltage E_d	400 V
Grid frequency f_g	50 Hz
Sampling frequency f_s	10 kHz
Inverter side inductance L_1	2 mH
Grid-side inductance L_2	1 mH
Filter capacitor C	10 μF
Damping resistance R	10 Ω

is identified as (0, 60). In this paper, $k_{c1} = 20$ is selected to achieve a balance between dynamic response and system instability.

The pole diagram with k_p varying independently as shown in Fig. 12(b). A properly selected proportional gain k_p can accelerate the convergence of the estimation error in the FA-RC-ESO. However, an excessively large k_p may introduce oscillations in disturbance estimation, thereby degrading system stability. As observed in Fig. 12(b), the effective operating range for k_p is identified as (0, 10000). In this paper, $k_p = 2500$ is chosen to balance dynamic performance and stability.

The pole diagram and Bode plot, with k_{r1} varying independently, are illustrated in Fig. 12(c) and Fig. 13, respectively. As shown in Fig. 13, with the increase of parameter k_{r1}, the phase lag of the FA-ADRC at its resonant frequency is gradually reduced. This reduction in phase lag effectively decreases the steady-state error of the system in reference current tracking. However, as shown in Fig. 12(c), higher values of k_{r1} also degrade system stability, as indicated by the poles distribution. Considering both tracking accuracy and system stability, $k_{r1} = 350$ is selected in this paper.

V. EXPERIMENTAL VERIFICATION

To verify the effectiveness of the proposed FA-ADRC scheme, a single-phase GCI experimental platform with an LCL filter is established, as shown in Fig. 14. In Fig. 14, the dc bus voltage is supplied by a Gwinstek APS-2302 programmable dc power supply. The inverter platform is a Yanxu YXPHM-TP3xb-I. The grid voltage u_g, encompassing background harmonics, is generated by a Chroma 61815 programmable power grid simulator. The power quality analyzer is a Fluke 1775, the microcontroller is a TMS320F28335 and the current sensor is an LAH 25-NP. The experimental parameters are listed in Table I. To simulate the practical power grid environment, a distorted grid voltage with THD= 5.7% is generated using the power grid simulator. The spectrum analysis of grid voltage is shown in Fig. 15.

In subsequent experiments, the QR-ADRC [14] control schemes based on the improved control law, the MQR-ESO-ADRC [22], TDF-ADRC [24], and NRC-ESO-ADRC [6]

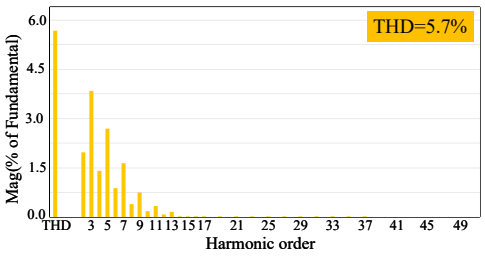

Fig. 15. The spectrum analysis of grid voltage.

schemes based on the improved ESO, and the proposed FA-ADRC are sequentially implemented for comparative analysis.

The parameters of the QR-ADRC are as follows: $k_c = 2000$, $b_0 = 333.333$, the observer bandwidth $w_0 = 8000$ rad/s, the resonant gains $k_r = 10$, the resonant bandwidth $w_c = 10$ rad/s, the resonant angular frequency $w_r = 314$ rad/s. The QR-ESO with five resonant controllers is designed, and the parameters of the MQR-ESO-ADRC are as follows: $k_c = 10000$, the observer bandwidth $w_0 = 2900$ rad/s, the resonant bandwidth $w_c = 10$ rad/s, the resonant angular frequencies $w_{r1} = 314$ rad/s, $w_{r3} = 3w_{r1}$ rad/s, $w_{r5} = 5w_{r1}$ rad/s, $w_{r7} = 7w_{r1}$ rad/s and $w_{r9} = 9w_{r1}$ rad/s, respectively; the resonant gains $k_{r1} = 0.05$, $k_{r3} = 0.03$, $k_{r5} = 0.02$, $k_{r7} = 0.01$, and $k_{r9} = 0.05$, respectively. The parameters of the TDF-ADRC are as follows: $b_0 = 333.333$, $k_c = 10000$, $k_p = 1000$, the observer bandwidth $w_0 = 1500$ rad/s, the RC gain $k_{rc} = 2500$. The parameters of the NRC-ESO-ADRC are as follows: $k_c = 2500$, $k_p = 10000$ and $b_0 = 333.333$. The parameters of the FA-ADRC are as follows: $b_0 = 333.333$, $k_p = 10000$, $k_c = 20 \times b_0$, the resonant gain $k_r = 350 \times b_0$, the resonant bandwidth $w_c = 3.14$ rad/s.

A. Steady-State Performance Verification under Voltage Distortions

The steady-state performance of the proposed FA-ADRC is verified through different experiments. When the amplitude of the reference current I_{ref} is 10 A and the grid frequency f_g is 50 Hz, the injected current waveforms, the output voltage waveforms, the injected current errors, and the injected current spectrums of the QR-ADRC, MQR-ESO-ADRC, TDF-ADRC, NRC-ESO-ADRC, and FA-ADRC are shown in Fig. 16, respectively.

The injected current THD of the QR-ADRC, MQR-ESO-ADRC, TDF-ADRC, NRC-ESO-ADRC and FA-ADRC are 12.1%, 3.8%, 2.7%, 1.0% and 0.9%, respectively, while the corresponding injected current errors are ±2.5 A, ±1.25 A, ±3.25 A, ±0.4 A, and ±0.4 A, respectively. The experimental results demonstrate that among the five control schemes, the proposed FA-ADRC achieves the best steady-state performance, exhibiting the lowest THD of 0.9% and the smallest steady-state error of ±0.4 A. In contrast, the QR-ADRC shows the poorest performance, with a significantly higher THD of 12.1% and a large steady-state error of ±2.5 A. It is worth noting that although the TDF-ADRC achieves a THD of 2.7%, its 24th, 26th, and 49th harmonic components significantly exceed the IEEE Std. 519-2022 limits and fail

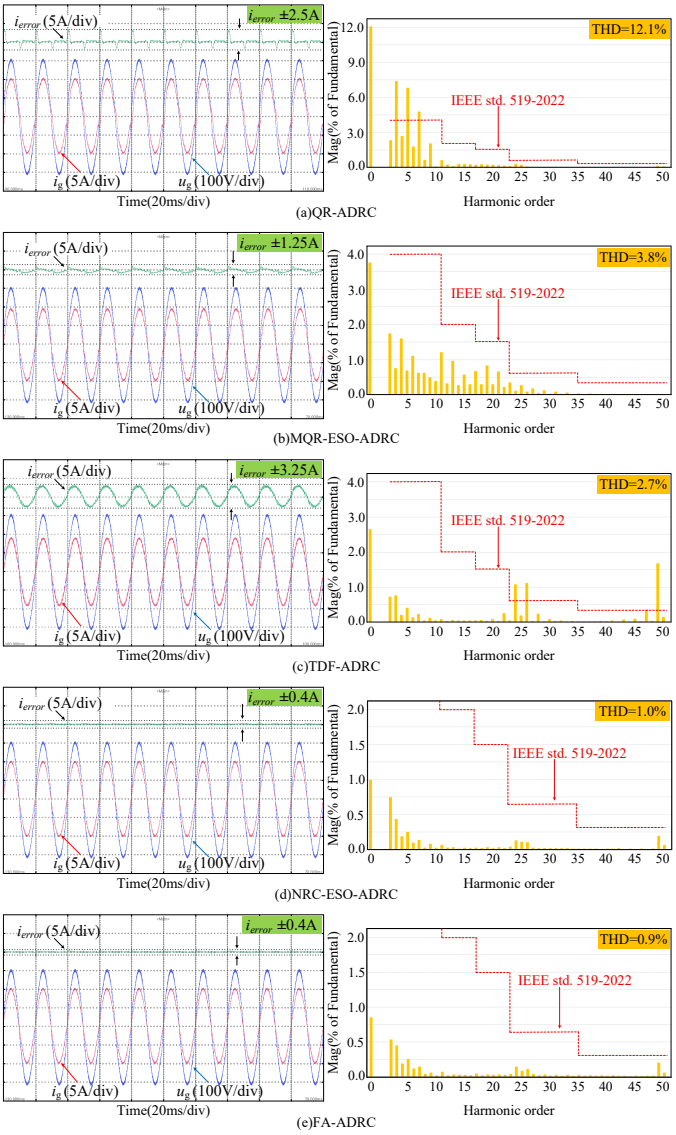

Fig. 16. Output waveforms and spectral analysis of the grid current i_g in different controllers with $I_{ref} = 10$ A.

to meet the required specifications. This is attributed to the use of a constant gain $Q(z)$ in the TDF-ADRC, which lacks frequency-selective attenuation capability, resulting in poor suppression of high-frequency measurement noise. In contrast, the proposed FA-ADRC adopts a zero-phase low-pass filter structure for $Q(z)$, effectively limiting the observer bandwidth. This design not only ensures accurate estimation of low-frequency disturbances but also significantly attenuates high-frequency noise components.

To intuitively demonstrate the harmonic suppression capability of the FA-ADRC under distorted grid voltage conditions, five control schemes are evaluated under grid voltage THD levels of 0.2%, 5.7%, and 9.2%, respectively. The corresponding injected current THD values are summarized in Table II.

From the Table II, it is evident that the proposed FA-ADRC consistently achieves the lowest current THD. Specifically, when the grid voltage THD is 0.2%, FA-ADRC limits the current THD to 0.5%. Even under severe voltage distortion

TABLE II
CURRENT THD OF DIFFERENT CONTROL SCHEMES UNDER GRID VOLTAGE DISTORTION

Methods	THD of $u_g = 0.2\%$	THD of $u_g = 5.7\%$	THD of $u_g = 9.2\%$
QR-ADRC [14]	2.7%	12.1%	20.2%
MQR-ESO-ADRC [22]	2.3%	3.8%	7.7%
TDF-ADRC [24]	1.9%	2.2%	2.5%
NRC-ESO-ADRC [6]	0.6%	1.0%	1.1%
Proposed FA-ADRC	0.5%	0.9%	1.0%

of 9.2%, FA-ADRC maintains the current THD at only 1.1%, significantly outperforming other methods such as MQR-ESO-ADRC (7.7%) and QR-ADRC (20.2%).

B. Frequency Robustness Verification

The frequency robustness of the proposed FA-ADRC is verified through different experiments. When the grid frequency f_g is 50.4 Hz and the amplitude of the reference current I_{ref} steps from 5 A to 10 A, the injected current waveforms, output voltage waveforms, injected current steady-state errors, power factors and current THD values of the QR-ADRC, MQR-ESO-ADRC, TDF-ADRC, NRC-ESO-ADRC, and FA-ADRC are illustrated in Fig. 17, respectively. It should be noted that the power factor λ, grid current THD, and current error i_{error} shown in the Fig. 17 are measured under the conditions of a grid frequency of 50.4 Hz, a reference current of 10 A.

As shown in Fig. 17, among the control schemes based on the improved ESO, FA-ADRC, NRC-ESO-ADRC, and MQR-ESO-ADRC reach steady-state within approximately 40 ms when subjected to a sudden reference current change, whereas TDF-ADRC requires nearly 100 ms to stabilize. Moreover, the FA-ADRC maintains a minimal stesdy-state error of ±0.4 A and achieves a THD of 0.9%, which is significantly lower than those of the other three methods. Additionally, the FA-ADRC attains a power factor λ of 0.999, indicating near-perfect synchronization with the grid voltage waveform. In contrast, TDF-ADRC, NRC-ESO-ADRC, and MQR-ESO-ADRC exhibit larger steady-state current errors of ±5 A, ±3.5 A, and ±1.5 A, respectively, with corresponding THD values of 5.8%, 5.7%, and 3.8%. Although the QR-ADRC scheme based on the improved control law achieves the fastest transient response, with a settling time of approximately 1 ms, it significantly underperforms the proposed FA-ADRC in steady-state accuracy and harmonic suppression, exhibiting a steady-state error of ±2.5 A and a THD of 12.1%. These experimental results confirm that FA-ADRC provides superior frequency-domain robustness under grid frequency fluctuations, enabling precise current tracking and effective harmonic mitigation.

To intuitively demonstrate the harmonic suppression performance of the proposed FA-ADRC under grid frequency fluctuations, the five control schemes are experimentally evaluated when the grid frequency varied sinusoidally with an amplitude of 0.1 Hz, within the range of 50±0.4 Hz. The corresponding grid current THD results are presented in Fig. 18. As shown in Fig. 18, the THD values of the QR-ADRC,

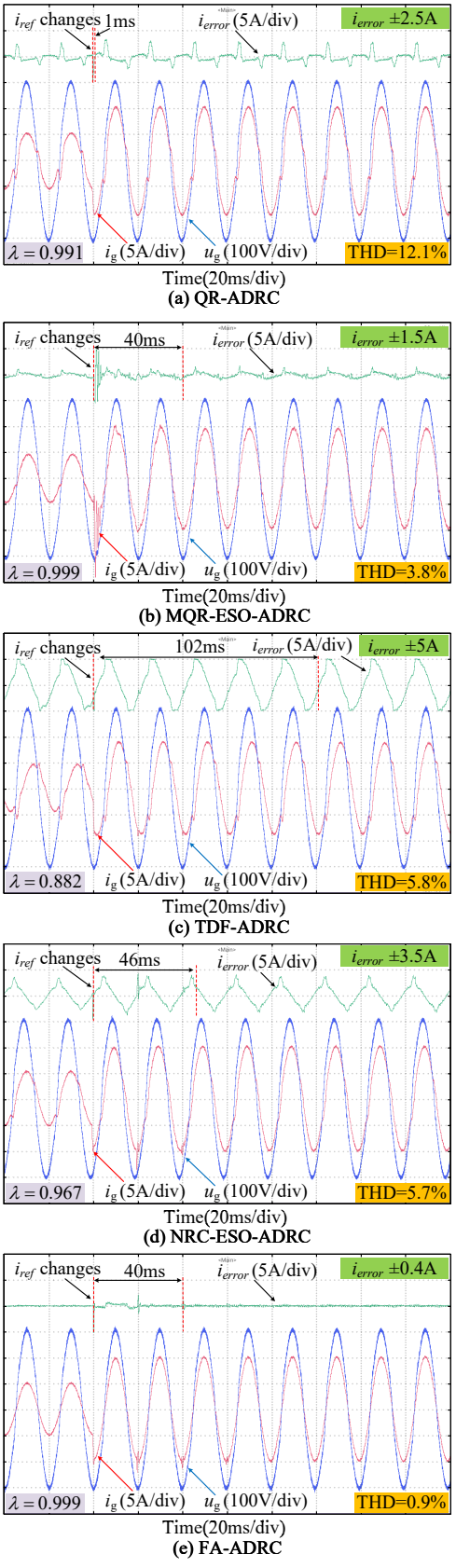

Fig. 17. Output waveforms of different controllers when the reference current steps from 5 A to 10 A.

TABLE III
PERFORMANCE COMPARISON OF DIFFERENT CONTROL SCHEMES

Method	Harmonic Suppression Capability	Frequency Adaptability	Steady-State Error	Noise Suppression Capability	Parameter Tuning Complexity	Average Computation Time	Memory
QR-ADRC [14]	Weak	Weak	Large	Strong	High	1.04 μs	0.086 KB
MQR-ESO-ADRC [22]	Weak	Moderate	Large	Strong	High	3.06 μs	0.223 KB
TDF-ADRC [24]	Moderate	Weak	Large	Weak	High	2.54 μs	1.64 KB
NRC-ESO-ADRC [6]	Strong	Weak	Small	Strong	Low	2.73 μs	1.65 KB
Proposed FA-ADRC	Strong	Strong	Small	Strong	Low	4.38 μs	2.63 KB

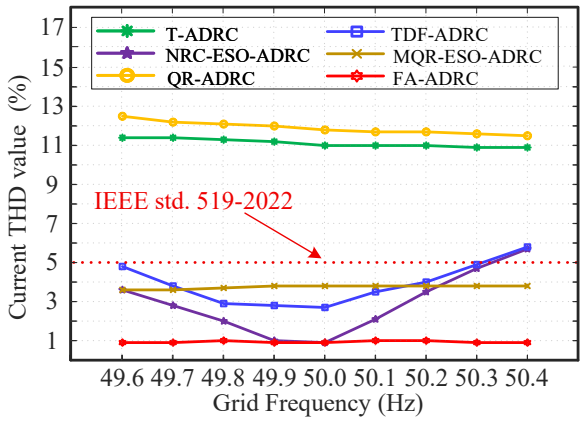

Fig. 18. The current THD of different schemes under frequency fluctuations.

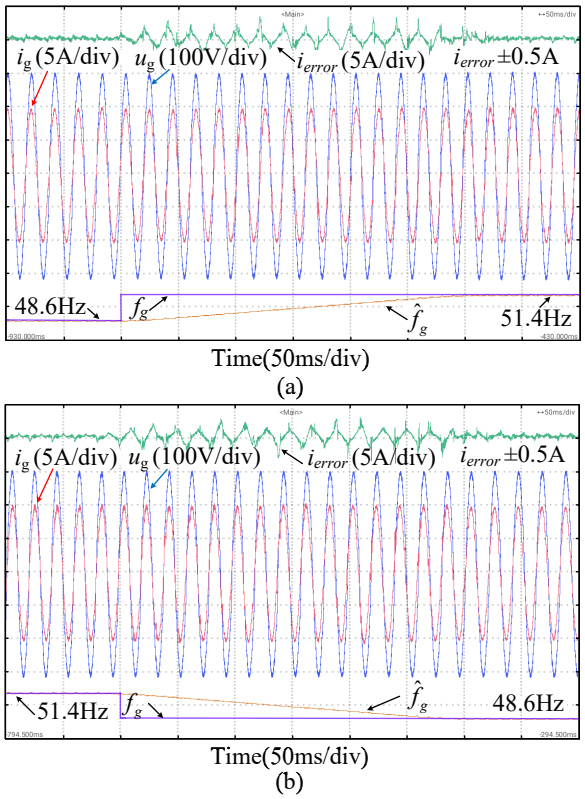

Fig. 19. The current waveform under grid frequency steps.

T-ADRC, MQR-ESO-ADRC, TDF-ADRC, and NRC-ESO-ADR schemes increase substantially under grid frequency fluctuations, reaching peak values of 12.3%, 11.2%, 3.8%, 5.8%, and 5.7%, respectively. In contrast, the proposed FA-ADRC consistently maintains the lowest THD, with minimal sensitivity to frequency fluctuations, effectively suppressing harmonic distortion below 1.1% and significantly outperforming the other five methods.

Furthermore, to evaluate the control performance of the proposed FA-ADRC under wide grid frequency fluctuations, two experiments are conducted: one with a step increase in grid frequency from 48.6 Hz to 51.4 Hz (Fig. 19(a)), and the other with a step decrease from 51.4 Hz to 48.6 Hz (Fig. 19(b)). As shown in Fig. 19, when the grid frequency fluctuates, the injected current gradually responds and reaches steady state after approximately 300 ms, with the steady-state error limited to within ±0.5 A. In practical applications, grid frequency fluctuations typically occur at a slow rate [33], thus, the dynamic response exhibited under this condition is adequate to satisfy real-world operational requirements.

C. Grid Impedance Uncertainty Verification

In order to verify the control performance of the proposed FA-ADRC under conditions of uncertain grid impedance, experiments are conducted with different grid impedances, at a grid frequency of 50 Hz. The THD of the injected current of the FA-ADRC system is shown in the table IV. As shown in Table IV, when L_g varies from 0 mH to 4 mH, the injected current THD consistently remains around 1.0%.

TABLE IV
CURRENT THD UNDER DIFFERENT GRID IMPEDANCE

The value of L_g (mH)	0	1	2	3	4
THD of i_g (%)	0.9	0.9	0.9	1.0	0.9

The experimental results indicate that the FA-ADRC exhibits strong robustness to parameter variations.

D. Comparative Analysis with Existing Methods

To clearly demonstrate the performances of the proposed FA-ADRC scheme, a comparative Table III is presented, which systematically compares FA-ADRC with several enhanced ADRC schemes [6], [14], [22], [24], in terms of harmonic suppression capability, frequency adaptability, steady-state error, noise suppression capability, parameter tuning complexity, average computation time, and memory. The proposed

FA-ADRC achieves strong harmonic suppression, superior frequency adaptability (uniquely "Strong"), and low steady-state error while retaining robust noise rejection and low tuning complexity, outperforming prior methods. Although its runtime is marginally longer due to sliding-window PLL filtering and IIR-based frequency adaptation, the computational load remains within real-time constraints. The slight increase in average computation time is justified by its unparalleled performance across all metrics, ensuring practical viability without compromising real-time operation. Thus, the FA-ADRC represents a balanced trade-off, where minor computational overhead is offset by significant control-performance advancements.

VI. Conclusion

To address the performance degradation and limited frequency adaptability of RC-ESO-ADRC schemes in single-phase GCIs under weak grids, this paper proposes a novel FA-ADRC scheme. The proposed scheme introduces a novel FA-RC-ESO structure based on an IIR filter to improve harmonic disturbance estimation accuracy when the grid frequency fluctuates. Furthermore, an FA-QPR controller is designed to enhance reference tracking performance. Experimental results verify that the proposed FA-ADRC achieves a lower THD and stronger frequency robustness compared to conventional methods, demonstrating its effectiveness and feasibility for weak and distorted grid applications. However, the steady-state performance of the FA-ADRC depends on the accuracy of grid frequency extraction, and there is an inevitable trade-off between accuracy and response speed in frequency extraction.

In future work, the proposed FA-ADRC scheme can be extended to three-phase GCI systems operating under weak grid conditions. Compared to the single-phase case, such extensions may face additional challenges including synchronization with multi-phase systems, increased control complexity due to multiple current loops, and the need for more precise PLL mechanisms. Furthermore, the implementation may require multiple current and voltage sensors, raising hardware cost and system integration complexity. In addition, adaptive parameter tuning techniques, such as machine learning-based gain adjustment, can be investigated to further enhance controller robustness under dynamically changing grid impedance and harmonic conditions.

References

[1] X. Wang, K. Qin, X. Ruan, D. Pan, Y. He, and F. Liu, "A robust grid-voltage feedforward scheme to improve adaptability of grid-connected inverter to weak grid condition," *IEEE Trans. Power Electron.*, vol. 36, no. 2, pp. 2384-2395, Feb. 2021.

[2] M. Zhu, Y. Ye, Y. Xiong, and Q. Zhao, "Parameter robustness improvement for repetitive control in grid-tied inverters using an IIR filter," *IEEE Trans. Power Electron.*, vol. 36, no. 7, pp. 8454-8463, Jul. 2021.

[3] Q. Zhao, G. Zhou, Y. Xia, Y. Zhu, D. Yu, and H. Zhang, "Feedforward dual-mode repetitive control for single-phase V2G inverters in residential grids," *IEEE Trans. Transp. Electrif.*, doi: 10.1109/TTE.2025.3568818.

[4] Q. Zhao, H. Zhang, Y. Xia, Q. Chen, and Y. Ye, "Equivalence relation analysis and design of repetitive controllers and multiple quasi-resonant controllers for single-phase inverters," *IEEE J Emerg Select Topic Power Elect.*, vol. 13, no. 3, pp. 3338-3349, Jun. 2025.

[5] *IEEE Standard for Harmonic Control in Electric Power Systems*, IEEE Standard 519-2022. Aug. 2022.

[6] Q. Zhao, Q. Wang, H. Zhang, Y. Xia, and Y. Ye, "A novel RC-ESO-ADRC for harmonics suppression and robustness improvement of grid-tied inverters in a weak and distorted grid," *IEEE Trans. Power Electron.*, vol. 40, no. 9, pp. 12581-12593, Sept. 2025.

[7] Y. Yang, S.-C. Tan, and S. Y. R. Hui, "Adaptive Reference Model Predictive Control With Improved Performance for Voltage-Source Inverters," *IEEE Trans. Control Syst. Technol.*, vol. 26, no. 2, pp. 724-731, Mar. 2018.

[8] C. Cheng, S. Xie, L. Tu, L. Tan, Q. Qian, and J. Xu, "Single grid-current sensor-controlled weak-grid-following inverters: A state-and-disturbance observer-based robust control scheme achieving grid-synchronization and disturbance rejection," *IEEE Trans. Power Electron.*, vol. 37, no. 11, pp. 13743-13754, Nov. 2022.

[9] Q. Teng, G. Xu, X. Zheng, H. Mai, X. Ma, and Y. Wang, "A novel sliding mode observer-based compound sliding mode current control with active damping for single phase grid-tied inverter system in weak grid," *Int. J. Electr. Power Energy Syst.* vol. 141, Oct. 2022.

[10] C. Cheng, S. Xie, Q. Qian, J. Lv, and J. Xu, "Observer-based single-sensor control schemes for LCL-filtered grid-following inverters," *IEEE Trans. Ind. Electron.*, vol. 70, no. 5, pp. 4887-4900, May. 2023.

[11] J. K. Singh et al., "Active disturbance rejection control of photovoltaic three-phase grid following inverters under uncertainty and grid voltage variations," *IEEE Trans. Power Del.*, vol. 38, no. 5, pp. 3155-3168, Oct. 2023.

[12] A. Benrabah, D. Xu, and Z. Gao, "Active disturbance rejection control of LCL-filtered grid-connected inverter using Padé approximation," *IEEE Trans. Ind. Appl.*, vol. 54, no. 6, pp. 6179-6189, Nov. 2018.

[13] Y. Cao, Q. Zhao, Y. Ye, and Y. Xiong, "ADRC-based current control for grid-tied inverters: Design, analysis, and verification," *IEEE Trans. Ind. Electron.*, vol. 67, no. 10, pp. 8428-8437, Oct. 2020.

[14] S. Zhuo, Y. Ma, X. Liu, R. Zhang, S. Jin, and Y. Huangfu, "Quasi-resonant-based ADRC for bus voltage regulation of hybrid fuel cell system," *IEEE Trans. Ind. Electron.*, vol. 72, no. 1, pp. 439-448, Jan. 2025.

[15] Y. Cui, Z. Yin, P. Luo, D. Yuan, and J. Liu, "Linear active disturbance rejection control of IPMSM based on quasi-proportional resonance and disturbance differential compensation linear extended state observer," *IEEE Trans. Ind. Electron.*, vol. 71, no. 10, pp. 11910-11924, Oct. 2024.

[16] Z. Wang, J. Zhao, L. Wang, M. Li, and Y. Hu, "Combined vector resonant and active disturbance rejection control for PMSLM current harmonic suppression," *IEEE Trans. Ind. Inform.*, vol. 16, no. 9, pp. 5691-5702, Sep. 2020.

[17] B. Wang, M. Tian, Y. Yu, Q. Dong, and D. Xu, "Enhanced ADRC with quasi-resonant control for PMSM speed regulation considering aperiodic and periodic disturbances," *IEEE Trans. Transp. Electrif.*, vol. 8, no. 3, pp. 3568-3577, Sep. 2022.

[18] D. Huang, D. Min, Y. Jian, and Y. Li, "Current-cycle iterative learning control for high-precision position tracking of piezoelectric actuator system via active disturbance rejection control for hysteresis compensation," *IEEE Trans. Ind. Electron.*, vol. 67, no. 10, pp. 8680-8690, Oct. 2020.

[19] S. Fang, J. Meng, Y. Meng, Y. Wang, and D. Huang, "Discrete-time active disturbance rejection current control of PM Motor at low speed using resonant sliding mode," *IEEE Trans. Transp. Electrif.*, vol. 9, no. 3, pp. 4783-4794, Sep. 2023.

[20] A. A. Godbole, J. P. Kolhe, and S. E. Talole, "Performance analysis of generalized extended state observer in tackling sinusoidal disturbances," *IEEE Trans. Control Syst. Technol.*, vol. 21, no. 6, pp. 2212-2223, Nov. 2013.

[21] R. Miklosovic, A. Radke, and Z. Gao, "Discrete implementation and generalization of the extended state observer," in *Proc. IEEE Amer. Control Conf.*, pp. 2209-2214, 2006.

[22] X. Yang, H. Hu, H. Hu, Y. Liu, and Z. He, "A quasi-resonant extended state observer-based predictive current control strategy for three-phase PWM rectifier," *IEEE Trans. Ind. Electron.*, vol. 69, no. 12, pp. 13910-13917, Dec. 2022.

[23] J. Xu, Z. Wei, and S. Wang, "Active disturbance rejection repetitive control for current harmonic suppression of PMSM," *IEEE Trans. Power Electron.*, vol. 38, no. 11, pp. 14423-14437, Nov. 2023.

[24] S. Lin, Y. Cao, C. Li, Z. Wang, T. Shi, and C. Xia, "Two-degree-of freedom active disturbance rejection current control for permanent magnet synchronous motors," *IEEE Trans. Power Electron.*, vol. 38, no. 3, pp. 3640-3652, Mar. 2023.

[25] M. Tian, B. Wang, Y. Yu, Q. Dong, and D. Xu, "Discrete-time repetitive control-based ADRC for current loop disturbances suppression of PMSM drives," *IEEE Trans. Power Electron.*, vol. 18, no. 5, pp. 3138-3149, May. 2022.

[26] P. Pal, R. K. Behera, and U. R. Muduli, "Feedforward Repetitive Approach to Disturbance Rejection in DAB Converters for EV Charging," *IEEE Trans. Ind. Electron.*, doi: 10.1109/TIE.2024.3519565.
[27] H. Cao et al., "Improved deadbeat predictive current control of PMSM drives with repetitive control-based disturbance correction observer," *IEEE Trans. Power Electron.*, vol. 40, no. 1, pp. 801-812, Jan. 2025.
[28] S. Chen, Q. Zhao, Y. Ye, and B. Qu, "Using IIR filter in fractional order phase lead compensation PIMR-RC for grid-tied inverters," *IEEE Trans. Ind. Electron.*, vol. 9, no. 70, pp. 9399-9409, Sep. 2023.
[29] J. Ye, L. Liu, J. Xu, and A. Shen, "Frequency adaptive proportional-repetitive control for grid-connected inverters," *IEEE Trans. Ind. Electron.*, vol. 68, no. 9, pp. 7965-7974, Sep. 2021.
[30] V. Valimaki and T. I. Laakso, "Principles of fractional delay filters," *in Proc. IEEE Int. Conf. Acoust., Speech, Signal Process.*, Istanbul, Turkey, 2000, vol. 6, pp. 3870–3873.
[31] M. Tomizuka, "Zero phase error tracking algorithm for digital control," *ASME Trans. J. Dyn. Syst. Meas. Control*, vol. 109, no. 1, pp. 65–68, Mar. 1987.
[32] Q. Zhao and Y. Ye, "A PIMR-type repetitive control for a grid-tied inverter: Structure, analysis, and design," *IEEE Trans. Power Electron.*, vol. 33, no. 3, pp. 2730-2739, Mar. 2018.
[33] *Voltage characteristics of electricity supplied by public distribution systems*, IEC 50160, 2022-12.